

RESEARCH ARTICLE

10.1002/2016JA023682

A high-resolution model of the external and induced magnetic field at the Earth's surface in the Northern Hemisphere

Key Points:

- Disturbance polar equivalent currents types 1 and 2 (*DP1* and *DP2*) resolved at 5 min cadence in all LT sectors and all polar latitudes via EOF
- *DP1* and *DP2* shown to collectively account for 65% of the total external and induced magnetic field variance in the polar region
- Data predictions based on the EOF reanalysis were used to derive time series of the polar cap radius in two local time sectors

Correspondence to:

R. M. Shore,
robore@bas.ac.uk

Citation:

Shore, R. M., M. P. Freeman, J. A. Wild, and J. W. Gjerloev (2017), A high-resolution model of the external and induced magnetic field at the Earth's surface in the Northern Hemisphere, *J. Geophys. Res. Space Physics*, 122, 2440–2454, doi:10.1002/2016JA023682.

Received 10 NOV 2016

Accepted 24 JAN 2017

Accepted article online 30 JAN 2017

Published online 17 FEB 2017

R. M. Shore¹ , M. P. Freeman¹ , J. A. Wild² , and J. W. Gjerloev^{3,4}

¹British Antarctic Survey, Cambridge, UK, ²Physics Department, Lancaster University, Lancaster, UK, ³Applied Physics Laboratory, The Johns Hopkins University, Laurel, Maryland, USA, ⁴Birkeland Center of Excellence, Department of Physics and Technology, University of Bergen, Bergen, Norway

Abstract We describe a method of producing high-resolution models of the Earth's combined external and induced magnetic field using the method of empirical orthogonal functions (EOFs) applied to the SuperMAG archive of ground-based magnetometer data. EOFs partition the variance of a system into independent modes, allowing us to extract the spatiotemporal patterns of greatest dynamical importance without applying the a priori assumptions of other methods (such as spherical harmonic analysis, parameterized averaging, or multivariate regression). We develop an approach based on that of Beckers and Rixen (2003) and use the EOF modes to infill missing data in a self-consistent manner. Applying our method to a north polar case study spanning February 2001 (chosen for its proximity to solar maximum and good data coverage), we demonstrate that 41.7% and 9.4% of variance is explained by the leading two modes, respectively, describing the temporal variations of the disturbance polar types 2 and 1 (*DP2* and *DP1*) patterns. A further 14.1% of variance is explained by four modes that describe separate aspects of the motion of the *DP1* and *DP2* systems. Thus, collectively over 65% of variance is described by the leading six modes and is attributable to *DP1* and *DP2*. This attribution is based on inspection of the spatial morphology of the modes and analysis of the temporal variation of the mode amplitudes with respect to solar wind measures and substorm occurrence. This study is primarily a demonstration of the technique and a prelude to a model spanning the full solar cycle.

1. Introduction

The magnetosphere and ionosphere are host to electrical current systems which are highly variable in space and across a wide range of time scales, ultimately driven by solar disturbances that wax and wane with an 11 year cycle and the associated turbulent interplanetary medium [e.g., Baumjohann and Treumann, 1997; Schunk and Nagy, 2009]. The cumulative magnetic field from these source currents is referred to as the external magnetic field, which contributes to all magnetic field measurements made at and above the Earth's surface.

Variations in the external magnetic field induce currents in the Earth's crust, mantle, and oceans, which create an additional contribution to the surface magnetic field. The surface external and induced magnetic field (EIMF) represents one of the largest sources of correlated error in state-of-the-art efforts to model the Earth's magnetic environment, such as the International Geomagnetic Reference Field (IGRF) [Thébault et al., 2015] and Comprehensive Models [Sabaka et al., 2015]. Since the surface EIMF is most variable throughout the polar regions, these areas are represented with disproportionate inaccuracy in magnetic models. Variability in the external magnetic field is also responsible for geomagnetically induced currents in man-made conducting infrastructure, notably electrical power grids, which can be a nuisance or hazard [Thomson et al., 2010].

From decades of study, it has been deduced that the polar EIMF can be decomposed into two main patterns the disturbance polar (*DP*) 1 and 2 patterns [Nishida, 1968a], along with other contributions including the solar quiet (*Sq*) [Matsushita et al., 1973], *DPY* [Friis-Christensen and Wilhelm, 1975], and *NBZ* patterns [e.g., Maezawa, 1976; Iijima et al., 1984].

Traditionally, an EIMF pattern is presented in terms of equivalent current, which is the ionospheric current confined within a spherical surface at around 100 km altitude that would create the EIMF, or even more simply the corresponding overhead uniform plane current (i.e., 90° clockwise to the local EIMF). We shall use this concept here, too. Under conditions of uniform conductivity and vertical magnetic field, the equivalent

current corresponds to the actual Hall current [Fukushima, 1969]. Otherwise, additional information on the Hall and Pedersen conductivities, electric field, or magnetic field-aligned current (FAC) is required to identify the source currents [e.g., Friis-Christensen *et al.*, 1985; Laundal *et al.*, 2015].

The DP2 pattern is a two-cell current pattern with relatively intense eastward and westward equivalent currents in the afternoon and morning magnetic local time (MLT) sectors, respectively. It is highly correlated at short (approximately 10 min) time lag with the southward component (B_z) of the interplanetary magnetic field (IMF) [Nishida, 1968b] and forms due to the interaction of the IMF and geomagnetic field as the solar wind moves antisunward past the Earth. This interaction—involving magnetic reconnection at the magnetopause and in the magnetotail—imposes a horizontal electric field in the polar ionosphere [Dungey, 1961]. This drives Pedersen currents which close region 1 and 2 FACs across auroral zone and (dependent on ambient conductivity) the region 1 FACs across the polar cap [Laundal *et al.*, 2015, 2016].

The DP1 pattern predominantly comprises an intense westward equivalent current across the midnight MLT sector. It is associated with a current wedge formed by the diversion of the cross-magnetotail current into the ionosphere at the onset of a substorm [McPherron *et al.*, 1973]. Consequently, it has a weak correlation with IMF B_z due to the fact that substorm onset timing has a complicated (time-integrated) relationship with the IMF [Freeman and Morley, 2004].

In this paper, we describe a method for obtaining a high-resolution model of the surface EIMF and demonstrate it in the north polar region. We utilize a mathematical technique commonly employed in meteorology, called empirical orthogonal functions (EOFs), to identify the natural time-varying patterns of the EIMF—its modes of variability. The EOF method is an eigenanalysis of the variance of a data set, designed to decompose it into a small number of independent spatial patterns and associated temporal oscillations [Jolliffe, 2002]. The EIMF is a system characterized by high variance (in both space and time), which lends itself to description by EOFs.

The primary benefit of EOF analysis is that it is able to describe the spatial and temporal morphology of the EIMF without applying strong a priori assumptions of these morphologies. This is in contrast to the two other methods typically used in geomagnetic field analysis. First, spherical harmonic analysis (SHA) assumes both a priori coordinate system and pattern geometry. SHA is commonly used in internal (and comprehensive) magnetic field models since it adeptly resolves the dipole-dominated, slowly varying internal field. To reduce the number of parameters required to resolve the more rapidly varying external field, these contributions can be described in a range of inertial coordinate systems of varying spatial or temporal complexity (e.g., CM5) [Sabaka *et al.*, 2015]. The choice of coordinate system can lead to a systematic loss of signal in the SHA model (e.g., demonstrated by Macmillan and Olsen [2013]), exacerbated by the low degree and order terms used to describe external variations (a result of the aforementioned parameter reduction). For example, the centroid of the auroral oval is offset antisunward of the Corrected Geomagnetic pole [Holzworth and Meng, 1975], thus requiring high SH degrees to represent the electrojet currents contained in the oval. Furthermore, the EIMF is spatially highly structured, such that even high-order models like CM5 cannot adequately capture the effect of the electrojet current reversal at the poleward edge of the auroral oval, or of the substorm electrojet, which both vary on order 100 km scale (approximately equivalent to spherical harmonic degree 100). The second main modeling method we consider is that based on conditional averages of the EIMF [e.g., Weimer, 2005a, 2005b; Weimer *et al.*, 2010; Weimer, 2013]. This approach may offer higher resolution but assumes that the variation of the EIMF can be explained by a few independent (e.g., IMF B_z) or dependent parameters (e.g., AE and Dst).

From ground-based magnetic data, Sun *et al.* [1998] and Xu and Kamide [2004] have used EOF-related methods to analyze the natural modes of variability in the polar region, while Balasis and Egbert [2006] have likewise assessed the midlatitude variability. The approach of Sun *et al.* [1998] was to fit a smooth SHA model to discrete measurements then apply the EOF analysis to the data predictions, leading to a loss of some signal. The other two studies each translated the data to the local time frame—Xu and Kamide [2004] performed this step for a single observatory and Balasis and Egbert [2006] ignored gaps between stations when applying the translation. In each case, the authors applied temporal filtering to constrain the errors introduced by their approaches. Here we develop a different method designed to be applied to a data set of a solar cycle's worth of magnetic vector measurements at 1 min resolution, at over 300 different locations around the world. These data have recently been collected by the international project SuperMAG [Gjerloev, 2012], spanning the years 1980 to 2015 at the time of writing. Following Beckers and Rixen [2003], our method self-consistently infills

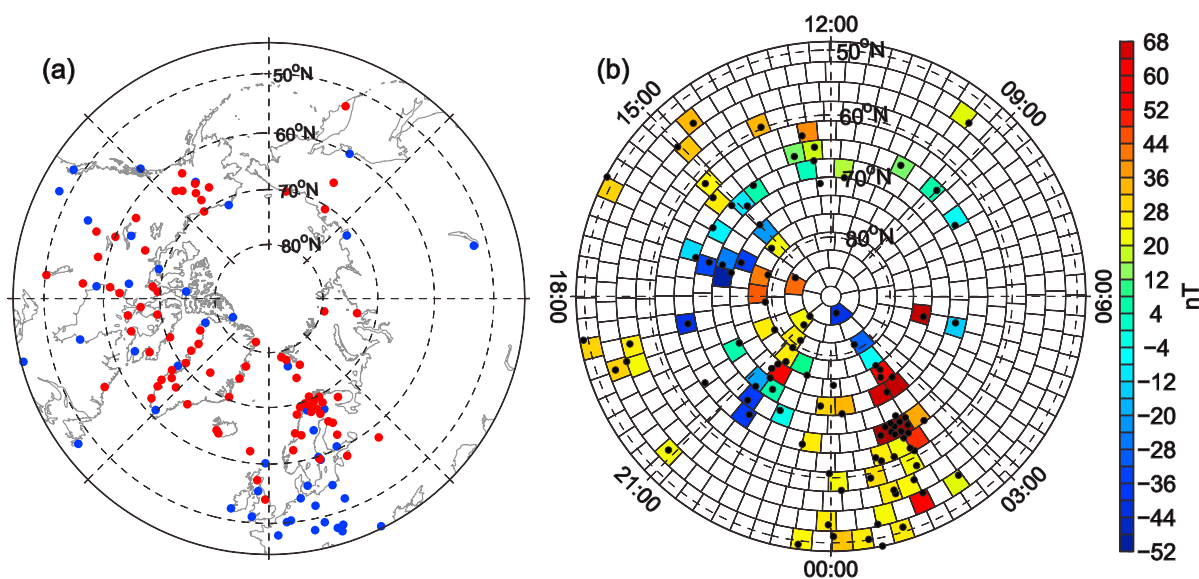


Figure 1. (a) Layout of the SuperMAG station locations in geographic coordinates which contributed data during 2001. Permanent observatories (numbering 47) are shown as blue dots, variometers (78) as red dots. (b) Example of the bin layout for the first 5 min of February 2001. Bin colors relate to the magnitude of the binned data—empty bins are white. Here the stations are shown in QD coordinates.

missing EIMF data based on the discovered modes. In this paper we demonstrate the method and its capabilities to resolve and decompose the EIMF in the polar regions for a sample month of data from the SuperMAG archive.

In section 2 we discuss the preprocessing of the SuperMAG data and the details of the subsequent EOF analysis method. In section 3 we present the results of the analysis and additional calculations supporting an interpretation of the discovered modes, consistent with existing knowledge. We discuss pros and cons of the method in section 4. We summarize our findings in section 5.

2. Method

2.1. Preanalysis Processing

The SuperMAG data set contains 1 min measurements from both permanent magnetic observatories (referenced to an absolute baseline) and magnetic variometers (variations about an arbitrary baseline). The northern polar distribution of the 125 stations available in February 2001 is shown in Figure 1a. We first reference the data to a common baseline, for which we use the existing SuperMAG rebaselining technique described by Gjerloev [2012] aimed at separating internal and external field contributions. We remove only the slowly varying “yearly” trend described by Gjerloev [2012], retaining signal up to time scales of about 1 month, with minimal bias from the core field secular variation.

The EOF analysis assumes that the signal of interest comprises a fixed set of spatial patterns of time-varying amplitude, i.e., standing waves. Thus, the EIMF signal will be represented by fewer EOF modes if we process the magnetic vector data in a coordinate system in which its spatial structure is relatively constant. This is similar to the parameter-reduction procedure used in SHA (described above), differing in that the EOF modes have no constraints on spatial complexity (beyond the resolution implied by the data coverage). For magnetosphere-ionosphere (MI) current systems driven by solar influence (e.g., Sq, DP1, DP2, and ring current) the optimal reference frame will be a Sun-synchronous coordinate system of magnetic latitudes. The choice of which magnetic latitudes to use can have a strong impact on the outcome of the analysis. Other authors [Milan et al., 2015] have used coordinate systems which move with the short-period variation of the external fields, in an attempt to account for expansion of the MI current systems (e.g., by defining latitudes relative to the auroral oval position). We have not done this since we seek to minimize assumptions in our discovery of the modes, and accounting for the external field motion incorrectly can introduce spatial errors from unfounded assumptions of the behavior of the system. Thus, we approach our analysis using magnetic latitudes defined from the internal magnetic field and process the EIMF data in the quasi-dipole (QD) system

[Richmond, 1995], using MLT rather than QD longitude. The use of QD coordinates (rather than say solar magnetospheric) minimizes variations due to longitudinal internal field variations in the MLT frame.

We rotate the magnetic vector measurements using the QD basis vectors, following the approach described in Emmert *et al.* [2010] and Laundal and Gjerloev [2014], resulting in the components (r , θ , and ϕ), directed, respectively, upward, southward, and eastward (approximately so, since the horizontal components are slightly nonorthogonal).

The EOF decomposition does not take the positions of the input data into account; hence, spatial clusters of stations can dominate the variance partitioning. To address such spatial clustering in the SuperMAG coverage, we create a set of approximately equal-area bins and equate the data value in each bin to the magnetic field value measured at the station closest to the centroid of the bin. Thus, only one station contributes to each bin at a given time, and there is some redundancy in the station coverage. We are therefore able to remove the contributions from stations which have (nonphysical) errors, without affecting the data coverage. We remove contributions from stations APL, ARC, CLK, DMH, EAG, GTF, HLL, KVI, PIN, and PKR prior to binning. The bins are fixed in the QD coordinate system, as illustrated for an example time in Figure 1b. The typical bin area is 110,000 km², chosen to maximize the invariant latitudinal resolution while satisfying that there is at least one station contributing to each bin (over the course of a given day). The details of the bin calculation procedure are described by Leopardi [2007].

To reduce processing costs, the 1 min resolution data from each station are combined (via taking their 5 min average) in 5 min spans prior to binning and set to nulls if any one of the five data points is missing in each span. The 5 min span is within the response time of the current systems of interest [e.g., Freeman, 2003], so the averaging procedure has little impact on the covariances. The binned data for a single magnetic field component comprise a data matrix of dimension n times by p spatial bins. Prior to the EOF analysis we subtract from each component the mean of each bin's time series (computed over n 5 min spans within each bin), since it is only the variance of the EIMF data which is analyzed. Rather than an EOF analysis being applied to each component separately, we treat the three components as extra parameters in the spatial dimension. Hence, the full mean-centered vector data matrix $\mathbf{X}_{o,g}$ is of size n by $3p$, where o is invariant and indicates "original" and g indicates the version of the binned data (in section 2.2, we will iteratively alter the binned data content). At this stage, $g = 1$.

The removed means $\bar{\mathbf{x}}$ are a vector of length p for each QD component. In this study we limit our interpretation to the θ and ϕ components, since these reflect the structure of the ionospheric equivalent currents. In Figure 2 we show the horizontal component of the background mean, the vectors rotated 90° clockwise to illustrate the direction, and magnitude of the equivalent ionospheric currents that would cause them. The θ component of the horizontal vector is used to color each bin—respectively, red (blue) indicate southward (northward) magnetic perturbations and westward (eastward) equivalent current flow. The pattern of the DP2 system dominates the background mean. Another notable feature in Figure 2 is the area of westward equivalent current at lower latitudes on the dayside thought to represent the northernmost edge of the Sq current system [Chapman and Bartels, 1940]. As we shall see later, this low-variance system does not have a significant contribution to the high-latitude modes.

The EOF decomposition requires that the input data set be complete, with no missing values. However, at any given epoch, most of the bins are empty. Throughout the analysis we will use a variety of values to complete the data matrix by infilling the missing data, and so any infilled (or complete) data matrix is referred to as a variant of $\mathbf{X}_{f,g,h}$. Here f is invariant and indicates that the data gaps are "filled," g refers (likewise to its definition above) to the version of the binned data to which the EOF analysis is applied (i.e., $g = 1$ for $\mathbf{X}_{o,1}$), and h refers to the iteration of the infill procedure, which we describe fully in section 2.2. As an initial infill choice we define a matrix $\mathbf{X}_{f,1,1}$, for which the null values of $\mathbf{X}_{o,1}$ are replaced by zeros (a reasonable guess value for the mean-centered data)

$$\begin{aligned} \mathbf{X}_{f,1,1} |_{\mathbf{x}_{o,g} \text{ exists}} &= \mathbf{X}_{o,1} \\ \mathbf{X}_{f,1,1} |_{\mathbf{x}_{o,g} \text{ null}} &= 0. \end{aligned} \quad (1)$$

For ease of reference, we define a "mask" matrix \mathbf{M} to assign null values to a given matrix, such that $\mathbf{X}_{o,g} = \mathbf{M}\mathbf{X}_{f,g,h}$. The processed data are now ready for EOF analysis.

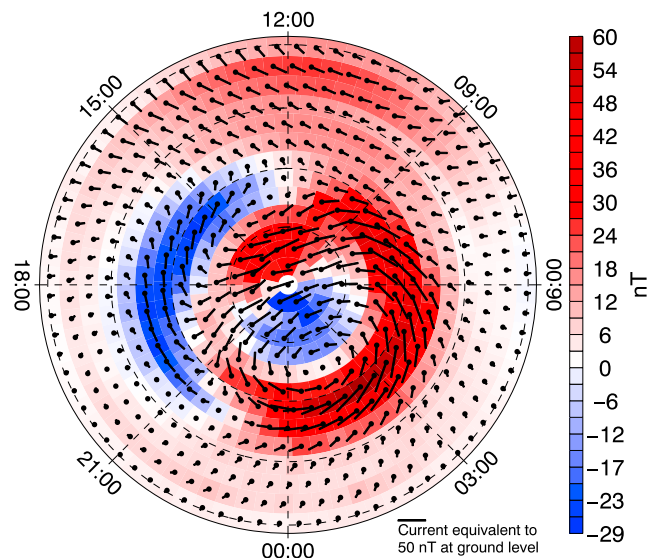


Figure 2. Spatial variation of the temporal mean of the horizontal component of the EIMF for February 2001. The data are shown in QD coordinates where the outer circle corresponds to 49° magnetic latitude and the labels around the outer circle indicate MLT. Color indicates the θ component of the mean magnetic field vector in each equal-area averaging region. Vectors stem from a dot at the centroid of each bin indicate the direction and strength of the corresponding equivalent currents. The binned data are means of 5 min averaged magnetic data, sampled to the QD-frame bins, after removal of baselines from each station time series.

2.2. Decomposition Method

As described by Bjornsson and Venegas [1997, p. 12], von Storch and Zwiers [2002, pp. 294–295], and Jolliffe [2002, p. 5], the principle of EOF eigenanalysis is that a mean-centered field $\mathbf{X}_{f,g,h}$ (comprising three-component data measured at a number of p locations for a number of n times) can be decomposed into n spatial patterns and n temporal oscillations. Each pair of a spatial pattern and its temporal oscillation is termed a “mode” of the analysis. The sum of the modes will reconstruct the variance of the original data. Each spatial pattern has three values at each of the p locations, reflecting the differing contribution of each component to the mode. If we define each spatial pattern \mathbf{v} as a column vector of length $3p$ (all modes represented collectively by $\mathbf{V} = (\mathbf{v}_1, \mathbf{v}_2, \dots, \mathbf{v}_n)$) and each temporal oscillation \mathbf{t} as a column vector of length n (represented collectively by $\mathbf{T} = (\mathbf{t}_1, \mathbf{t}_2, \dots, \mathbf{t}_n)$), then the decomposition of variance is given via

$$\mathbf{X}_{f,g,h} = \sum_j^n \mathbf{t}_j \mathbf{v}_j^T = \mathbf{TV}^T, \quad (2)$$

where the \mathbf{T} are the eigenvectors of \mathbf{R} , the covariance matrix of $\mathbf{X}_{f,g,h}$, formed from $\mathbf{R} = \mathbf{X}_{f,g,h} \mathbf{X}_{f,g,h}^T$. The \mathbf{V} are given by a projection of the eigenvectors onto the original data ($\mathbf{V} = \mathbf{X}_{f,g,h}^T \mathbf{T}$). The eigenvectors are a temporal basis, and this is referred to as a “T mode” analysis [Richman, 1986]. The proof that the basis vectors which diagonalize \mathbf{R} also maximize the variance of a projection onto \mathbf{X} is discussed by Hannachi *et al.* [2007] and von Storch and Navarra [1999].

The generalization of the (ostensibly scalar) EOF method to vector data is discussed by Jolliffe [2002], where it is termed common (or combined) principal component analysis. Although the EOF analysis takes no account of relationships between spatial parameters, our treatment of the QD components as additional parameters in the spatial dimension means that the three components of a given spatial pattern are each subject to the same temporal oscillation. For a set of amplitudes \mathbf{t}_i , the spatial amplitude for a given QD component is then controlled by the differing weights of the relevant third of the associated \mathbf{v}_i . Our approach greatly simplifies the physical interpretation of the modes and prevents the loss of information which can arise when the reconstruction (equation (2)) is truncated to the highest ranked modes by variance and when weaker components (e.g., ϕ) have a substantially lower ranking to the other components.

Our initial choice of zeros as infill values for missing data reduces the variance of the data set, and with it, the amplitude of the leading modes. Several different approaches to obtaining a complete data set from spatially

and temporally irregular measurements are possible. Since we have access to a good coverage of data, we are able to adopt an approach similar to that of *Beckers and Rixen* [2003] and iteratively use the output of the EOF analysis as a method for infilling empty bins, until convergence of the amplitudes of the modes and the data. We can use equation (2) to reconstruct the (infilled) data matrix for any combination of individual modes. We term the reconstruction of the first EOF mode $\mathbf{X}_{f,1,1}^e = \mathbf{t}_1 \mathbf{v}_1^T$. The values of $\mathbf{X}_{f,1,1}^e$ are used to refill the data matrix (afterward termed $\mathbf{X}_{f,1,2}$) via

$$\begin{aligned} \mathbf{X}_{f,1,2} \mid \mathbf{x}_{o,g} \text{ exists} &= \mathbf{X}_{o,1} \\ \mathbf{X}_{f,1,2} \mid \mathbf{x}_{o,g} \text{ null} &= \mathbf{X}_{f,1,1}^e \end{aligned} \quad (3)$$

The process of infilling $\mathbf{X}_{f,1,2}$ as per equation (3) and performing the EOF decomposition of equation (2) proceeds iteratively until the amplitude of $\mathbf{X}_{f,1,h}^e$ converges with that of $\mathbf{X}_{o,1}$, where both exist. We find that convergence occurs well within $h = 35$ for modes which contribute significantly to the total variance (discussed further in section 3.1), with diminishing returns for greater h . After convergence, the information represented by the leading mode is complete across all bins. We do not want this information to control the infill for subsequent modes, so we remove the iterated EOF solution from the original data via

$$\mathbf{X}_{o,2} = \mathbf{X}_{o,1} - \left(\mathbf{M} \mathbf{X}_{f,1,35}^e \right), \quad (4)$$

where $\mathbf{X}_{o,2}$ represents the original data minus the information contained in the first iterated mode. We then repeat the iterative infill process, beginning with zeros as before

$$\begin{aligned} \mathbf{X}_{f,2,1} \mid \mathbf{x}_{o,g} \text{ exists} &= \mathbf{X}_{o,2} \\ \mathbf{X}_{f,2,1} \mid \mathbf{x}_{o,g} \text{ null} &= 0 \end{aligned} \quad (5)$$

and upon solving $\mathbf{X}_{f,2,1}$ with the EOF analysis, use the reconstruction based on its leading mode to refresh the infill, repeating until $h = 35$. We have described a nested double iteration over g and h : we iteratively infill the empty bins using the amplitudes of the leading mode, then we correct the original data for this mode and repeat the process. The results discussed in this manuscript are the leading modes from each stage of the correction process, once convergence has been attained. Although all are technically “mode 1” of a given corrective stage, we refer to them as modes 1, 2, etc., according to the stage (i.e., value of g) they originated from. Although our EOF infill approach is based on that described by *Beckers and Rixen* [2003], the approaches differ slightly. While we iterate each mode to convergence and then subtract it from the original data, *Beckers and Rixen* [2003] infill gaps in the data using each mode in succession, without altering the original data. Our approach therefore slightly reduces the orthogonality of the leading modes we present since each originates from a different EOF analysis. This works to our benefit—since the current systems of interest are not mutually orthogonal, they are better separated when using our approach.

3. Results

3.1. Variance Explained

It is common to use the eigenvalues of the EOF decomposition as a direct measure of the amount of variance of the original undecomposed data “explained” by each mode. However, since our data include both measured and infilled values, the eigenvalues no longer have a direct relationship to the variance of the original data. The variance explained by a certain mode is calculated from the variance of $\mathbf{M} \mathbf{X}_{f,g,35}^e$ with g indicating the appropriate mode number. The variance of the original data is given from the variance of $\mathbf{X}_{o,1} = \mathbf{M} \mathbf{X}_{f,1,1}^e$. That is, the variances are calculated only at the measurement locations.

In Figure 3 we show a number of different representations of how each EIMF mode accounts for the variance of the measured data. The proportion of the variance of the measured data which is explained by each of the first 10 modes is shown in Figure 3a. This decreases rapidly from 42% for mode 1, 9% for mode 2, to less than 2% for modes 7 and higher. Modes 1 to 6 collectively account for over 65% of the variance of the measured data. While modes 7+ collectively define a not insignificant contribution to the variance, it is not clear that these modes are individually dominated by a single physical process, and thus, we cannot meaningfully interpret the patterns they represent. These modes are also less likely to converge during the infill process within a reasonable number of iterations. For these reasons we consider modes 1–6 to provide a reasonably complete and physically understandable description of the EIMF data, and these modes are the focus of our results below.

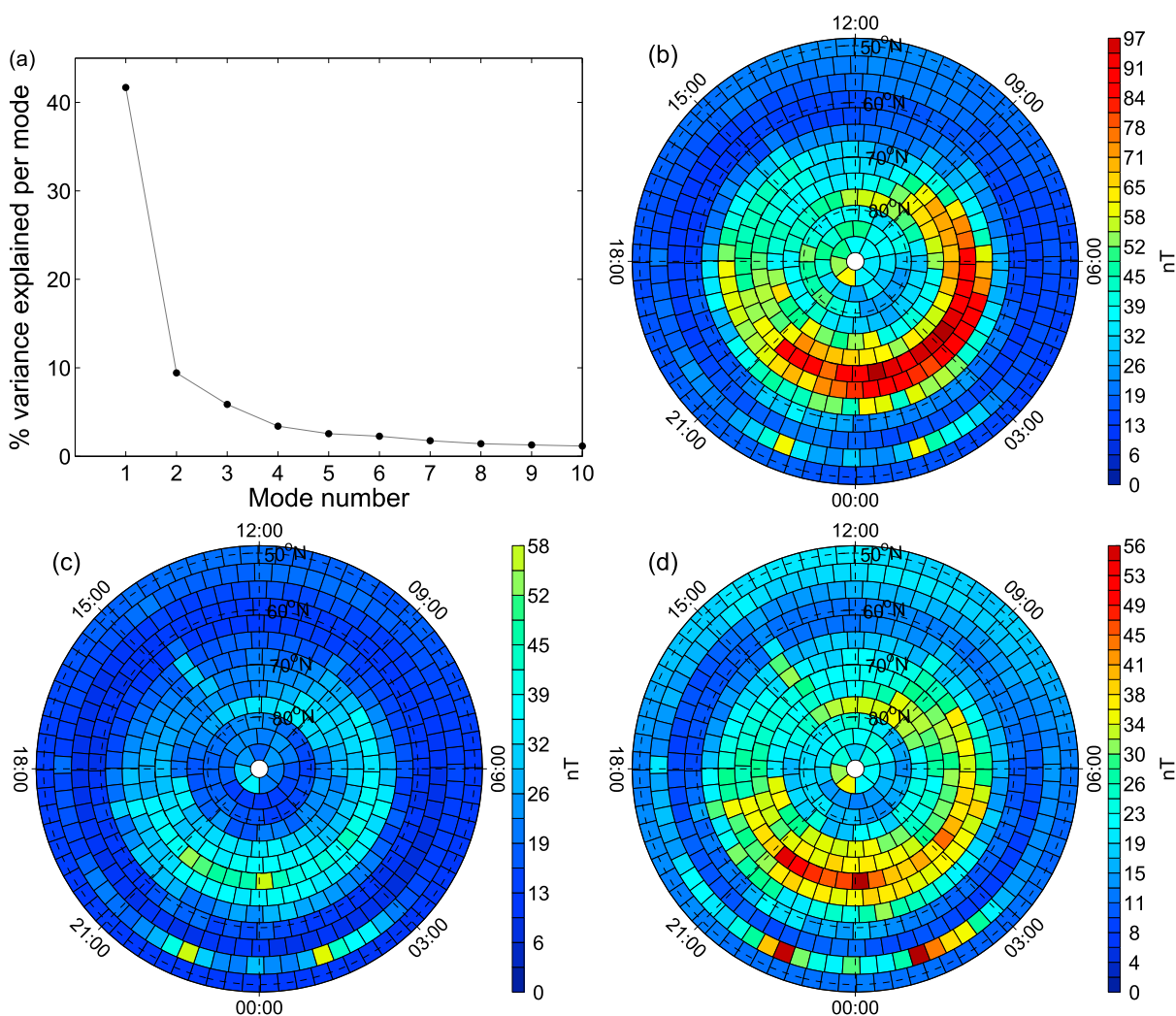


Figure 3. Various indicators of proportions of the original data explained by modes 1–10. (a) Proportion of variance of original data explained by modes 1–10. (b) RMS values of the original binned data. (c) RMS values of the original data minus prediction of modes 1–6, using the same color map as Figure 3b to aid comparison. (d) Same data as Figure 3c but using a color map which is saturated to the true range of the plotted data.

Figure 3b shows the horizontal vector norm of the RMS value of $\mathbf{X}_{o,1}$ inside each bin, exhibiting highest variability of the measured data in the postmidnight auroral region. In Figures 3c and 3d we show the horizontal vector norm of the RMS values of $\mathbf{X}_{o,1}$ once the reconstruction for modes 1 to 6 has been subtracted. We use the same color values in Figures 3b and 3c, but in Figure 3d we use a color scale which is saturated to the true range of the plotted data. Comparing Figures 3b and 3c, we see that the residuals have been reduced everywhere (as expected), and comparing Figures 3b and 3d, we demonstrate that the residual is roughly proportional to the original variance (i.e., the figures appear broadly similar). From this, we can deduce that the leading EOFs are adept at capturing the large-scale structures of variance in the data. The exception to this is in the premidnight MLT sector at auroral latitudes, where the leading EOF modes capture proportionately less of the EIMF variance than elsewhere, possibly due to the varying location of substorm onset [Frey *et al.*, 2004].

3.2. Decomposed Modes

The EOF decomposition returns EIMF modes which are not necessarily physically meaningful. However, in this analysis we are able to ascribe physical meaning to each of the EIMF modes 1–6, which we describe as follows.

3.2.1. EIMF Mode 1—The Static DP2 Current System

In Figure 4a we show, for the month of February 2001, the equivalent currents of the horizontal components of EIMF mode 1. The spatial pattern has been normalized such that multiplication of the pattern with its associated temporal oscillation (the middle panel in Figure 4a) will produce the appropriate perturbation for

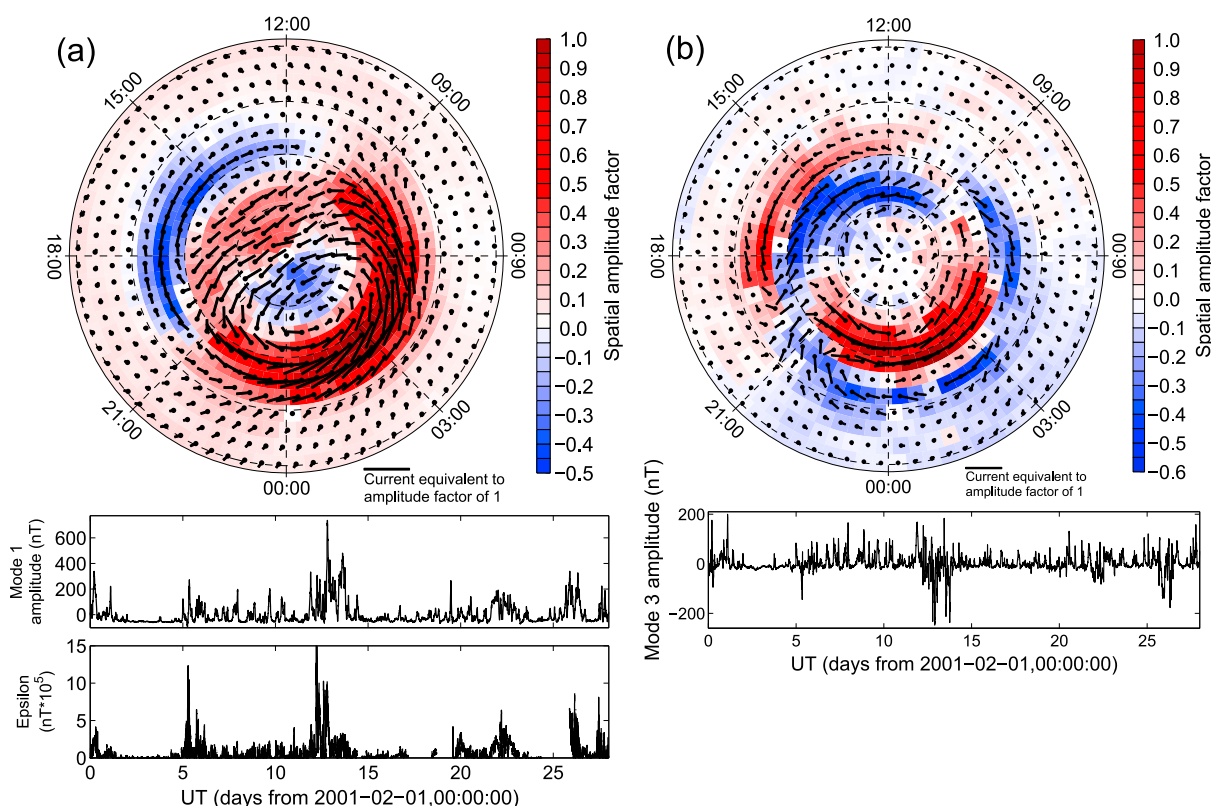


Figure 4. DP2 current modes. (a) Mode 1 normalized horizontal-component equivalent current spatial pattern with mode 1 temporal series and epsilon index shown underneath. (b) As the top two parts of Figure 4a but for mode 3. The equivalent current vectors and associated colors of the modes' spatial patterns are in the same format as Figure 2, except that here the vectors are normalized. The perturbation magnitude for the mode is given by the multiplication of the normalized EOF eigenvector with its associated temporal series.

that epoch. Similarly to Figure 2, the θ component of the EIMF mode (azimuthal equivalent current) is indicated by the color map—we adopt this presentation for each mode shown. The key feature of mode 1 is the two-cell spatial pattern of equivalent current flow, very similar to that of the mean field shown in Figure 2, which we interpreted as that of the DP2 current system (integrated over the analysis span of 1 month). To substantiate this, the lowermost panel in Figure 4a shows the epsilon index, an independent measure of the solar wind-magnetosphere coupling strength [Perreault and Akasofu, 1978; Akasofu, 1981; Koskinen and Tanskanen, 2002] that has been shown to correlate well with the polar electric field [Reiff *et al.*, 1981] associated with DP2 [Dungey, 1961]. The index is lagged by 30 min from the estimated time of first solar wind contact with the bow shock, to optimize comparison with our ground-based measurements. The lag of 30 min is in agreement with the range of lags shown by Sun *et al.* [1998] to best reflect the IMF impact at ground level. The time series of EIMF mode 1 and epsilon are similar, and indeed, mode 1 is found to have a temporal correlation (Pearson's r value of 0.61) with the lagged epsilon index. Although the variability of mode 1 is not strongly determined from the variability of epsilon (since the r^2 value is 0.37), the correlation is highly statistically significant ($p \ll 0.01$). Thus, based on the spatial and temporal patterns of mode 1, we consider it to represent the static part of the DP2 current system.

3.2.2. EIMF Mode 3—Expansion and Contraction of DP2

Any given mode of an EIMF decomposition is a standing mode (see equation (2))—it has a fixed spatial pattern such that the mode's perturbation varies proportionately everywhere with time. Thus, any spatial motions of the DP2 equivalent current system through the course of a month cannot be represented by a single mode, i.e., mode 1. Specifically, we know that spatial changes in DP2 result from expansions and contractions of the polar cap, dependent on the relative dominance of the dayside (magnetopause) and nightside (magnetotail) magnetic reconnection rates [e.g., Lockwood *et al.*, 1990].

We find that mode 3 describes the expansion and contraction of the DP2 pattern. The spatial pattern of mode 3, the equivalent currents of which are shown in Figure 4b, resembles the north-south spatial derivative

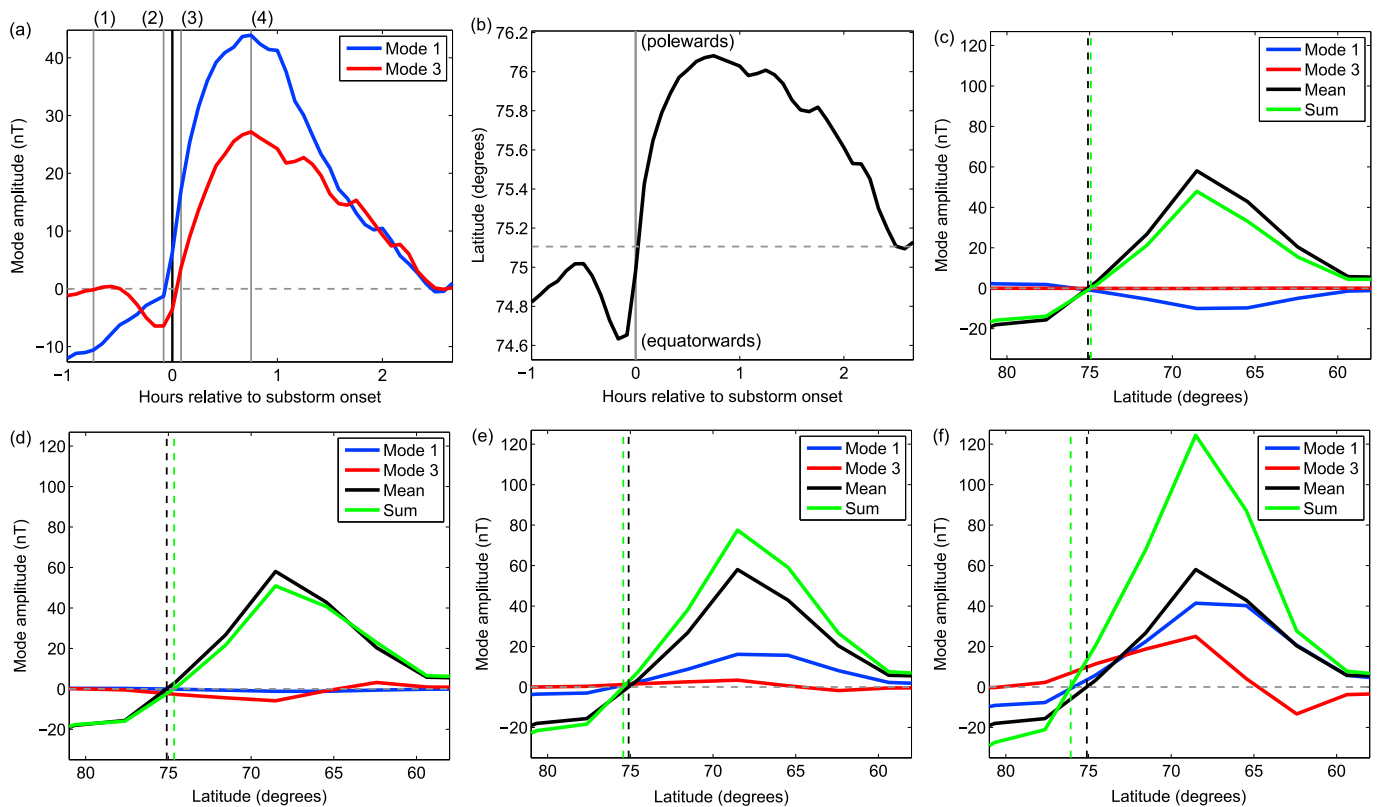


Figure 5. The average evolution of the $DP2$ equivalent currents given by modes 1 and 3 during a substorm. (a) The time series of mode 1 (blue) and mode 3 (red) amplitudes, individually superimposed and averaged with respect to the substorm onset epochs described in the main text. The thick black vertical line denotes the substorm epoch. Grey vertical lines labeled (1)–(4) indicate the reconstruction times at -40 , -5 , $+5$, and $+50$ min used in Figures 5c–5f, respectively. (b) Time series of the latitude at which the θ component crosses a value of zero for a sum of the background mean (Figure 2) and modes 1 and 3 (Figures 4a and 4b), each reconstructed using the mean mode amplitude shown in Figure 5a. The latitude of the zero crossing is computed at 02:10 MLT, the meridian where mode 1 peaks. The horizontal dashed line is the zero-crossing latitude of the background mean pattern. The vertical line indicates the substorm onset epoch. (c–f) Each panel shows a latitudinal cross section at 02:10 MLT of mode 1 (blue line), mode 3 (red), the background mean (black), and the sum of all these (green). Respectively, Figures 5c, 5d, 5e, and 5f correspond to the grey line (1), (2), (3), (4) in Figure 5a, illustrating the sequence of the substorm. The two vertical dashed lines in each panel are the zero-crossing latitudes of the mean (black) and sum (green) spatial patterns.

of mode 1 (not shown) and is dominant in the same LT sectors. Its full time series is shown in the lowermost panel in Figure 4b. Addition of mode 1 and mode 3 with varying weightings is found to cause mode 1 to expand or contract by varying amounts (not shown). This makes sense because the time rate of change of a field in a moving frame (e.g., $DP2$ expanding with the polar cap) is the addition of the time rate of change of the field at a fixed position (i.e., mode 1) and the spatial derivative of this field multiplied by the frame's velocity.

To describe the effect of an imbalance in dayside and nightside reconnection rates on $DP2$, we examine the behavior of modes 1 and 3 during substorms. As an independent indicator of substorm onset times, we use the epochs derived from IMAGE satellite data by *Frey et al.* [2004]. We have superimposed (separately and without duplication of data) the temporal variations of modes 1 and 3 with respect to each of the 87 substorm onsets in February 2001. In Figure 5a we show the mean of these superimposed time series, to highlight the change in strength of $DP2$ (from mode 1) and its motion (expansion/contraction from mode 3) throughout the typical substorm evolution. With respect to the monthly mean amplitude of $DP2$ of $+60$ nT (see Figure 2), mode 1 is weaker prior to onset and then rapidly stronger, and then more gradually weaker, after onset. We interpret this sequence to be the intensification in $DP2$ due to enhanced conductivity caused by particle precipitation from the magnetotail dipolarisation at onset [*Baumjohann and Treumann, 1997*]. The variation in mode 3 over the same time span is consistent with a relative expansion (negative amplitude) within 30 min prior to onset followed by a contraction in the following 2 h, consistent with the expanding-contracting model of polar cap evolution during the substorm [*Lockwood et al., 1990*]. To demonstrate this, in Figure 5b, we have summed the θ component spatial pattern of modes 1 and 3 (reconstructed for the superimposed substorm) in addition to the background mean (shown in Figure 2) and used this to calculate a time series of the latitude of

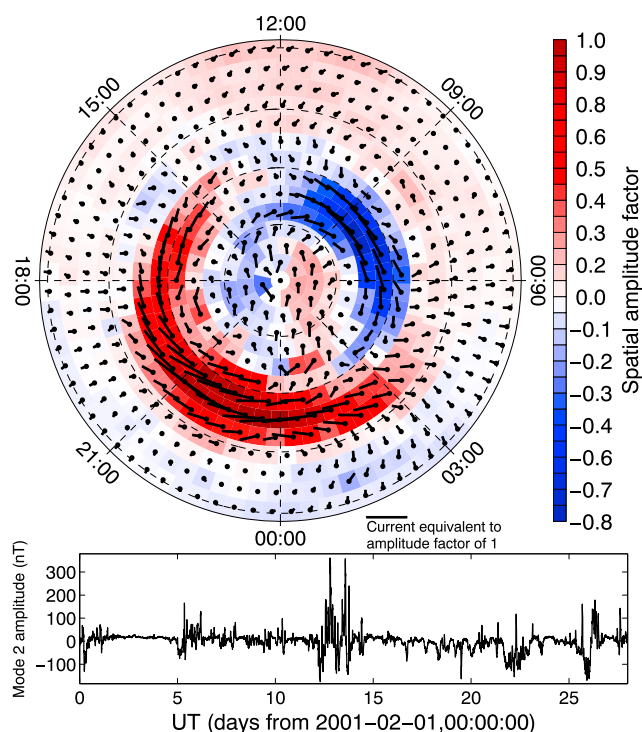


Figure 6. Mode 2 normalized spatial pattern and temporal series, in the same format as Figure 4b.

the polar cap boundary during the substorm. (To calculate this time series, we have linearly interpolated the spatial pattern of the summed modes to a meridian line at 02:10 MLT with a latitude spacing of 0.001° , and from this we compute the latitude at which the θ component crosses a value of zero.) The expansion and contraction of the polar cap shown in Figure 5b follows the trend of mode 3 in Figure 5a almost exactly. This is a strong verification of our interpretation of mode 3 as a mathematical description of the expansion and contraction of the DP2 pattern according to the polar cap size. Note that the latitudinal displacement is smaller than that expected for individual substorms because this is the average over many substorms, and indeed, larger displacements of the mode 1 and 3 pattern are seen for individual substorms (not shown).

Figures 5c–5f illustrate the meridional profiles of modes 1 and 3, the background mean, and the sum of these three, for successive epochs throughout the superimposed substorm corresponding to the lines labeled (1)–(4) in Figure 5a. From these, the relative contributions of modes 1 and 3 to the θ component zero crossing can be seen. In Figure 5c 40 min prior to the substorm growth phase, a weakened DP2 convection system is apparent with little expansion or contraction. Just (5 min) before substorm onset in Figure 5d, we see that mode 3 is negative, shifting the weak convection pattern equatorward. Almost immediately (5 min) after substorm onset in Figure 5e, mode 3 has changed sign and mode 1 has strengthened, increasing the magnitude of the DP2 pattern and moving it poleward. Finally, in Figure 5f 50 min after onset, we show the maximum amplitudes of modes 1 and 3, corresponding to the strongest perturbation of the DP2 equivalent current system and its most contracted (poleward) extent, prior to recovery (not illustrated). In this way, the sum of modes 1 and 3 is capable of describing much of the morphology of the DP2 system.

3.2.3. EIMF Mode 2—The Static DP1 Current System

The normalized spatial pattern of the mode 2 equivalent currents is shown in Figure 6, along with its amplitude time series. In the nightside, the spatial pattern exhibits a westward equivalent current which peaks in the premidnight LT sector and at auroral latitudes. We interpret this as the static part of the disturbance polar 1 (DP1) system of the substorm current wedge. This is substantiated in Figure 8a which shows the mean temporal evolution of the mode 2 amplitude with respect to substorm onset in the same way as in Figure 5a. The solid black curve in Figure 8a is given by

$$f(t) = cte^{pt} + b \quad |_{t \geq 0} \tag{6}$$

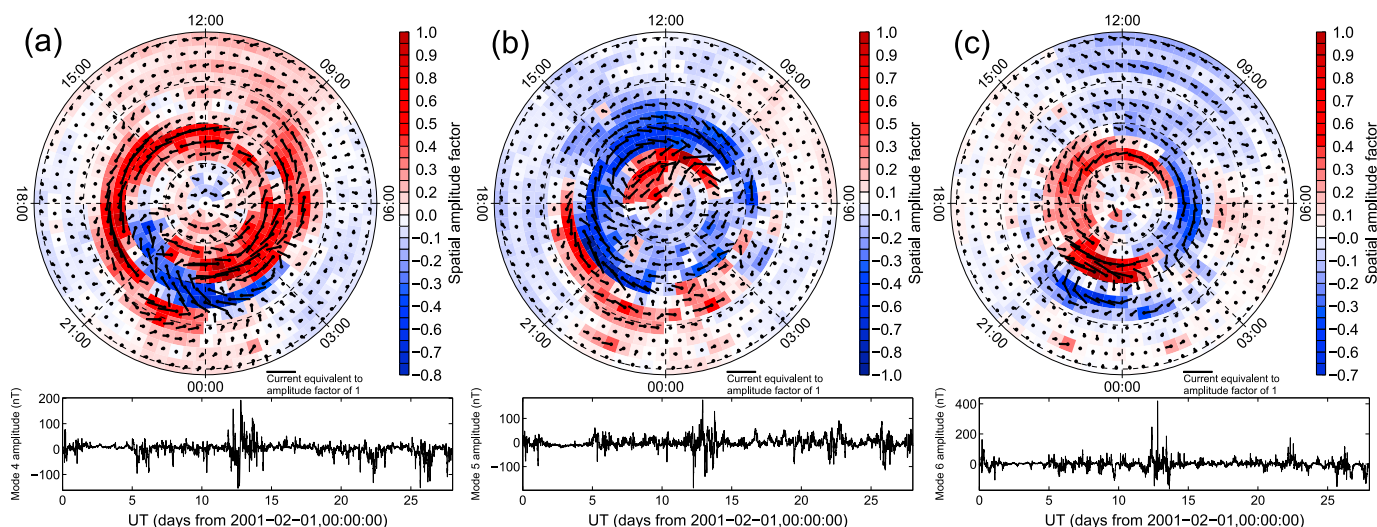


Figure 7. Normalized spatial patterns and temporal series for modes 4, 5, and 6, respectively, in Figures 7a, 7b, and 7c, each in the same format as Figure 4b.

where t indicates time since onset and the constants c , p , and b are calculated using a least squares procedure which best fits the mean mode 2 series (green line in Figure 8a). We obtain $c = 251.13$ nT and $p = 2.78$ h⁻¹. The functional form in equation (6) was shown by Weimer [1994] to fit a superposition of the (negative) AL index with respect to substorm onset and argued to be a solution of the current flowing in a resistive electrical circuit appropriate to the substorm current wedge. Weimer [1994] divided the AL index into three groups of increasing amplitude and obtained values for c from 794 to 3232 nT and p (after correction for sign) ranging from 1.78 to 2.42 h⁻¹. The good agreement between the black and green curves in Figure 8a and the relatively similar values of the time constant ($1/p$) indicates that mode 2 describes the general form of the substorm. The lower amplitude of c in our case may be due to the removal of the DP2 and other modes from the EIMF signal.

In Figure 6, the mode 2 pattern exhibits an eastward equivalent current, which peaks at auroral latitudes between 05:00 and 11:00 MLT. This eastward current is part of a more general trend seen between 03:00 and 20:00 MLT, in which the mode 2 pattern is approximately opposite to the mode 1 DP2 pattern (shown in Figure 4a) in the same sector. Since both modes 1 and 2 are increasingly positive after substorm onset (see Figures 5a and 8a), this indicates that substorm onset causes a localized increase in the amplitude of the DP2 equivalent current in the nightside 20:00 to 03:00 MLT sector with respect to the dayside 03:00 to 20:00 MLT sector. This is likely due to the enhancement of ionospheric conductivity in the 20:00 to 03:00 MLT sector by precipitating particles in the substorm current wedge causing an associated increase of DP2 in this nightside sector. Comparing the amplitudes of the mean (Figure 2), mode 1 (Figure 4a) and mode 2 (Figure 6) patterns at the end of the expansion phase (at approximately onset +20 min), we estimate that the nightside DP2 is enhanced by up to about 50% with respect to the dayside. Thus, while the DP1 system is distinct from DP2, they are not entirely independent in the EOF decomposition, and the dayside structure of mode 2 (including the eastward equivalent current) is a measure of the connection of these otherwise independent patterns.

3.2.4. EIMF Modes 4–6—Spatial Changes of DP1

While mode 2 describes the majority of the EIMF variance associated with a substorm, to capture the full effect of the substorm on DP1 requires a number of additional spatial patterns. We find that when combined with mode 2, modes 4–6 each describe some aspect of the change of the DP1 equivalent current system during a substorm. The equivalent currents of modes 4–6 are shown in normalized form in Figure 7. Mode 4 (shown in Figure 7a) describes an east-west motion of the peak of the nightside mode 2 equivalent current. Analogous to mode 3 and mode 1, we see that mode 5 (shown in Figure 7b) resembles the latitudinal derivative of mode 2 in the evening sector. Thus, mode 5 describes the poleward contraction of the mode 2 equivalent current in this sector. Similarly, mode 6 (shown in Figure 7c) describes the poleward motion of the poleward boundary of the DP1 equivalent current in the pre-midnight sector. Although modes 5 and 6 have somewhat similar physical effects on mode 2, it is mode 6 which is more spatially localized (near the mode 2 peak amplitude) and is of stronger amplitude than mode 5. Hence, mode 6 is more important than mode 5 to the expansion

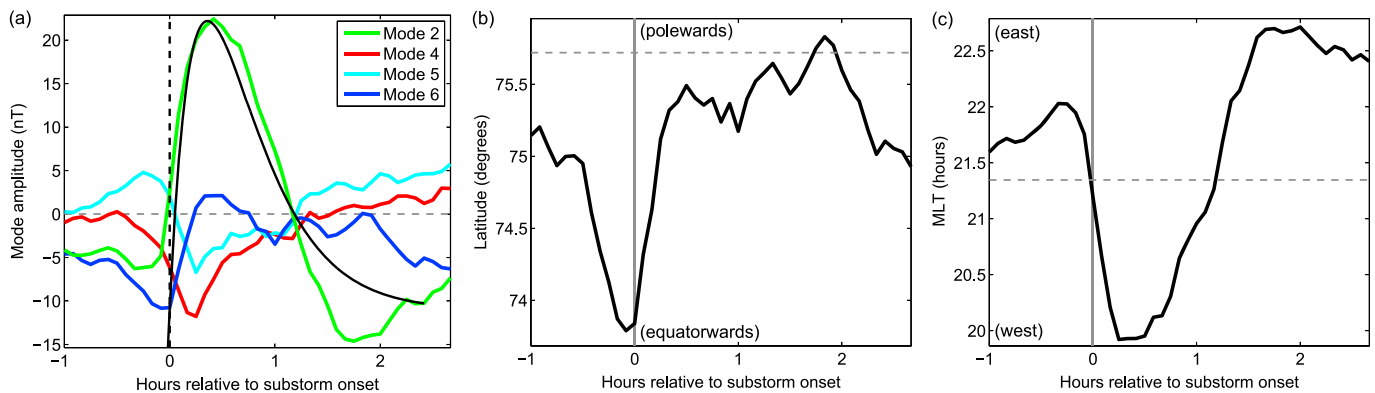


Figure 8. The average evolution of the *DP1* equivalent current modes 2, 4, 5, and 6 during a substorm. (a) The time series of each of the modes 2 (green), 4 (red), 5 (light blue), and 6 (dark blue) amplitudes has been individually superimposed and averaged with respect to the substorm onset epochs described in the main text. The black vertical line denotes the substorm epoch. The black solid curve is a model substorm response, given by equation (6). (b) Time series of the latitude at which the θ component crosses a value of zero for a sum of the background mean (Figure 2) and modes 2, 4, 5, and 6 (Figures 6 and 7), each reconstructed using the mean mode amplitude shown in Figure 8a. The latitudes are computed at 23:20 MLT, the meridian where the mode 2 amplitude peaks. The horizontal dashed line is the zero-crossing latitude of the background mean pattern. The vertical line indicates the substorm onset epoch. (c) Time series of the longitude (computed from $QD \text{ MLT} \times 15$) of the θ component zero crossing for the same sum of modes as in Figure 8b. The longitudes are computed at a latitude of 69° (approximately the mode 2 peak latitude) and between 18:00 and 24:00 MLT. The horizontal dashed line is the zero-crossing longitude of the background mean pattern. The vertical line indicates the substorm onset epoch.

and contraction of the *DP1* poleward boundary and associated polar cap boundary experienced during the substorm, as we show in the following analysis.

Figure 8b illustrates the latitude of the polar cap boundary during the superimposed substorm, along a meridian line at 23:20 MLT. The calculation process is similar to that described earlier for Figure 5b—we sum the θ components of modes 2, 4–6, and the background mean, then compute the zero-crossing latitude between the mode 2 peak amplitude and the pole. The time series of this latitude is similar to the temporal series of mode 6 during the superimposed substorm (the dark blue curve in Figure 8a), confirming our interpretation of this mode as the dominant descriptor of the expansion and contraction of the poleward edge of the westward equivalent current in this MLT sector. The rapid poleward motion of the zero-crossing latitude at substorm onset is consistent with the poleward expansion of the nightside aurora—a defining feature of the substorm expansion phase—and the contraction of the polar cap.

For the same sum of modes 2, 4–6, and the background mean, Figure 8c shows a time series of the longitude (computed from $QD \text{ MLT} \times 15$) of the zero crossing of the θ component at a latitude of 69° , between 18:00 and 24:00 MLT. This illustrates the tendency of the substorm equivalent current wedge to travel westward upon substorm onset. This is likely due to a combination of the background mean with modes 2 and 4, because (as described above) modes 5 and 6 are more associated with latitudinal motion.

The substorm evolution can be summarized as an intensification and westward surge of the premidnight sector westward equivalent current in the auroral oval, accompanied by a pronounced contraction of the polar cap. These aspects are described by the modes 2 and 4–6, collectively the descriptors of the *DP1* current system. On the dayside, the tendency of *DP2* to respond to the substorm creates spatial patterns in modes 2 and 4–6 which are not directly related to the substorm equivalent current wedge. Hence, we have based our interpretation of the physical meaning of the “*DP1* modes” on their responses in the nightside MLT sector. The sum of modes 1–6 provides a complete description of the winter polar cap dynamics.

4. Discussion

The EOF method has the following three main benefits. First and foremost is the self-consistency of the approach; since the EOF method is empirical, its solutions are determined by the data without requiring their morphology to be specified prior to analysis. This is of greatest practical use when using the modes themselves to infill missing values, as the process can only converge for infill solutions which reinforce the patterns in the data. Second, the discovered modes provide valuable insight into the major electrical currents affecting the EIMF system and the accompanying underlying physical processes. Third, the decomposition of a data set into independent modes allows for a substantially more compact description of its key attributes.

A comparison of the amplitudes of the removed means (Figure 2) to the much higher amplitudes of mode 1 (middle panel in Figure 4a) shows that the EIMF is a system dominated by its variance, which lends it naturally to decomposition by EOFs.

These types of benefits have led to EOFs being used recently in studies of other aspects of ionospheric electrodynamics, for instance, the electric field and plasma motion [Matsuo *et al.*, 2002; Kim *et al.*, 2012; Cousins *et al.*, 2013a, 2013b], field-aligned current [Cousins *et al.*, 2015; Milan *et al.*, 2015], and particle precipitation and associated conductivity [Stoneback *et al.*, 2013; McGranaghan *et al.*, 2015, 2016]. EOFs have also been applied to the geomagnetic field, as here, by Golovkov *et al.* [2007], Shore *et al.* [2016], and the studies examined above [Sun *et al.*, 1998; Xu and Kamide, 2004; Balasis and Egbert, 2006]. The closest study to ours is that of Sun *et al.* [1998], which used 70 ground-based magnetic stations, successfully resolved *DP2* and *DP1* over the whole polar cap, and demonstrated a correlation of the *DP2* system with epsilon. Our study improves upon this work in that Sun *et al.* [1998] used the method (described in the study of Kamide *et al.* [1982]) of SHA to create a continuous coverage of data prior to analysis by the method of EOFs. Our chosen infill approach relies only on the EOF method itself, thus is more self-consistent, and free from the spatial smoothing and geometric assumptions inherent in SHA. Our resolution of six distinct, physically meaningful modes to the two modes resolved by Sun *et al.* [1998] demonstrates the stability and accuracy of the iterative-infill approach described by Beckers and Rixen [2003] when applied to the SuperMAG data set.

We also highlight the recent study of Milan *et al.* [2015], which applied an eigen decomposition to the Active Magnetosphere and Planetary Electrodynamics Response Experiment (AMPERE) data set of field-aligned currents, in an analysis spanning 2010–2012. The method is applied to different data (and a different electromagnetic component) to our study, but aims to resolve essentially similar physical processes, and thus provides a useful complement to our results. Perhaps, the primary difference to our study is that Milan *et al.* [2015] have transformed their data into a coordinate system which expands and contracts according to the latitude of a circle fitted to the auroral oval. This is intended to simplify the data and enable more of it to be represented as standing waves. The step will reduce the absolute variance of the data set and should “steepen” the eigenspectrum, i.e., allow proportionally more of the variance to be accounted for by the leading modes. However, a comparison of our eigenspectrum (Figure 3a) with those presented by Milan *et al.* [2015] shows that a substantially greater proportion of the variance is accounted for by the first mode in our study (41% to approximately 25%). The correction applied by Milan *et al.* [2015] has apparently added to the complexity of the data rather than reducing it. This may also be the reason that the authors find no coherent substorm response, since the substorm will represent one of the larger deviations from a circular geometry for the auroral oval. The resolution by Milan *et al.* [2015] of a mode describing the dayside cusp currents is not seen in our analysis since for the winter month we present here, this system is very weak. This will be shown in a subsequent study, in preparation.

Despite the increasing popularity of the EOF method, it does have some downsides. The pre-EOF removal of the mean is a constraint in that it requires filtering of the data via the baseline approach. Yet the baseline has minimal variance over the course of a month and is added back on to any station-specific prediction for a given EOF mode. The primary constraint of EOFs in this case is their orthogonality, requiring that the decomposed patterns be uncorrelated. While this precludes the unique separation of correlated systems, it also exposes novel, unexpected information about the physical connections in the EIMF system. The connection between the *DP1* mode and the *DP2* mode on dayside was not expected but provides valuable insight into attempts to model the whole polar cap system.

The good similarity between the relationship in equation (6) and the mean of the superposed mode 2 time series corroborates our interpretation of mode 2 as the substorm component of the EIMF. We have utilized correlations with independent parameters of solar-terrestrial coupling to assist in our interpretations of the modes. As part of a wider investigation into the significance of each of the first six modes, we performed Pearson correlations (not shown) between the mode amplitude series and IMF B_x , IMF B_y , and the solar wind dynamic pressure (each lagged by 30 min). These exhibited no substantial correlation. IMF B_z (lagged by 30 min) showed a correlation of -0.58 with mode 1 ($p \ll 0.01$), but this is expected given the input of IMF B_z to the epsilon index. While mode 1 is certainly dominated by the *DP2* system, identification of the precise relationship of *DP2* to epsilon, and of the physical links between modes 1 and 2, requires the incorporation of further independent solar-terrestrial interaction parameters to data spanning a greater amount of time, and is left as a future study.

5. Conclusions

We have demonstrated that the method of EOFs is capable of describing the polar external and induced magnetic field from ground-based data, providing novel information on the spatiotemporal evolution of the key polar equivalent current systems. With the EOF method, the DP2 and DP1 systems, and modes describing their spatial fluctuations, are resolvable in all LT sectors and at all times. They describe over 65% of the total variance of the northern polar EIMF during the sample month studied (February 2001). We use this information to derive time series of the polar cap radius in two LT sectors as an example of the utility of the modes. Our results represent a substantial improvement on existing work and indicate that the method is highly suitable for a solar cycle length analysis of the EIMF, which is under way.

Acknowledgments

Funding for this project was provided by NERC grant NE/J020796/1. The work was performed using hardware and support at the British Antarctic Survey (BAS). Thanks go to Gareth Dorrian for discussions on the results which improved the project. MATLAB code for the rotation to QD coordinates was provided by Nils Olsen. MATLAB code used to compute the equal-area bin layout was written by Paul Leopardi. The epsilon, IMF, and solar wind dynamic pressure measures used in this study were calculated from OMNI data downloaded from ftp://spdf.gsfc.nasa.gov/pub/data/omni/high_res_omni/monthly_1min/ on 2014–02–28. The version used has been resampled to simulate measurements taken at the magnetopause. The results presented in this paper rely on ground magnetometer data supplied by the SuperMAG archive, for which we gratefully acknowledge: INTERMAGNET (we thank the national institutes that support its contributing magnetic observatories and INTERMAGNET for promoting high standards of magnetic observatory practice (www.intermagnet.org)); USGS, Jeffrey J. Love; CARISMA, PI Ian Mann; CANMOS; The S-RAMP Database, PI K. Yumoto and K. Shiokawa; The SPIDR database; AARI, PI Oleg Troshichev; The MACCS program, PI M. Engebretson, Geomagnetism Unit of the Geological Survey of Canada; GIMA; MEASURE, UCLA IGPP and Florida Institute of Technology; SAMBA, PI Eftyhia Zesta; 210 Chain, PI K. Yumoto; SAMNET, PI Farideh Honary; The institutes who maintain the IMAGE magnetometer array, PI Eija Tanskanen; PENGUIN; AUTUMN, PI Martin Connors; DTU Space, PI Juergen Matzka; South Pole and McMurdo Magnetometer, PI's Louis J. Lanzarotti and Alan T. Weatherwax; ICESTAR; RAPIDMAG; PENGUIN; British Antarctic Survey; MacMac, PI Peter Chi; BGS, PI Susan Macmillan; Pushkov Institute of Terrestrial Magnetism, Ionosphere and Radio Wave Propagation (IZMIRAN); GFZ, PI Juergen Matzka; MFGI, PI B. Heilig; IGPPAS, PI J. Reda; University of LAquila, PI M. Vellante; SuperMAG, PI Jesper W. Gjerloev.

References

- Akasofu, S. I. (1981), Energy coupling between the solar wind and the magnetosphere, *Space Sci. Rev.*, *28*(2), 121–190, doi:10.1007/BF00218810.
- Balasis, G., and G. D. Egbert (2006), Empirical orthogonal function analysis of magnetic observatory data: Further evidence for non-axisymmetric magnetospheric sources for satellite induction studies, *Geophys. Res. Lett.*, *33*, L11311, doi:10.1029/2006GL025721.
- Baumjohann, W., and R. Treumann (1997), *Basic Space Plasma Physics*, Imperial College Press, London.
- Beckers, J. M., and M. Rixen (2003), EOF calculations and data filling from incomplete oceanographic datasets, *J. Atmos. Oceanic Technol.*, *20*(12), 1839–1856.
- Bjornsson, H., and S. Venegas (1997), A manual for EOF and SVD analyses of climatic data, CCGCR (Centre for Climate and Global Change Research) Rep., 97(1), McGill Univ.
- Chapman, S., and J. Bartels (1940), *Geomagnetism*, vol. 1, Clarendon Press, Oxford.
- Cousins, E. D. P., T. Matsuo, and A. D. Richmond (2013a), Mesoscale and large-scale variability in high-latitude ionospheric convection: Dominant modes and spatial/temporal coherence, *J. Geophys. Res. Space Physics*, *118*(12), 7895–7904, doi:10.1002/2013JA019319.
- Cousins, E. D. P., T. Matsuo, and A. D. Richmond (2013b), SuperDARN assimilative mapping, *J. Geophys. Res. Space Physics*, *118*(12), 7954–7962, doi:10.1002/2013JA019321.
- Cousins, E. D. P., T. Matsuo, A. D. Richmond, and B. J. Anderson (2015), Dominant modes of variability in large-scale Birkeland currents, *J. Geophys. Res. Space Physics*, *120*(8), 6722–6735, doi:10.1002/2014JA020462.
- Dungey, J. W. (1961), Interplanetary magnetic field and the auroral zones, *Phys. Rev. Lett.*, *6*, 47–48.
- Emmert, J. T., A. D. Richmond, and D. P. Drob (2010), A computationally compact representation of magnetic-apex and quasi-dipole coordinates with smooth base vectors, *J. Geophys. Res.*, *115*, A08322, doi:10.1029/2010JA015326.
- Freeman, M. (2003), A unified model of the response of ionospheric convection to changes in the interplanetary magnetic field, *J. Geophys. Res.*, *108*(A1), 1024, doi:10.1029/2002JA009385.
- Freeman, M. P., and S. K. Morley (2004), A minimal substorm model that explains the observed statistical distribution of times between substorms, *Geophys. Res. Lett.*, *31*(12), L12807, doi:10.1029/2004GL019989.
- Frey, H. U., S. B. Mende, V. Angelopoulos, and E. F. Donovan (2004), Substorm onset observations by image-FUV, *J. Geophys. Res.*, *109*, A10304, doi:10.1029/2004JA010607.
- Friis-Christensen, E., and J. Wilhjelm (1975), Polar cap currents for different directions of the interplanetary magnetic field in the Y-Z plane, *J. Geophys. Res.*, *80*(10), 1248–1260, doi:10.1029/JA080i010p01248.
- Friis-Christensen, E., Y. Kamide, A. D. Richmond, and S. Matsushita (1985), Interplanetary magnetic field control of high-latitude electric fields and currents determined from Greenland magnetometer data, *J. Geophys. Res. Space Physics*, *90*(A2), 1325–1338, doi:10.1029/JA090iA02p01325.
- Fukushima, N. (1969), Equivalence in ground geomagnetic effect of Chapman–Vestine's and Birkeland–Alfvén's electric current-systems for polar magnetic storms, Tech. Rep., Tokyo Univ.
- Gjerloev, J. (2012), The SuperMAG data processing technique, *J. Geophys. Res.*, *117*, A09213, doi:10.1029/2012JA017683.
- Golovkov, V., T. Zvereva, and T. Chernova (2007), Space-time modeling of the main magnetic field by combined methods of spherical harmonic analysis and natural orthogonal components, *Geomagn. Aeron.*, *47*, 256–262.
- Hannachi, A., I. T. Jolliffe, and D. B. Stephenson (2007), Empirical orthogonal functions and related techniques in atmospheric science: A review, *Int. J. Climatol.*, *27*(9), 1119–1152, doi:10.1002/joc.1499.
- Holzworth, R. H., and C.-J. Meng (1975), Mathematical representation of the auroral oval, *Geophys. Res. Lett.*, *2*(9), 377–380, doi:10.1029/GL002i009p00377.
- Iijima, T., T. A. Potemra, L. J. Zanetti, and P. F. Bythrow (1984), Large-scale Birkeland currents in the dayside polar region during strongly northward IMF: A new Birkeland current system, *J. Geophys. Res.*, *89*(A9), 7441–7452, doi:10.1029/JA089iA09p07441.
- Jolliffe, I. T. (2002), *Principal Component Analysis*, 2nd ed., Springer, Berlin.
- Kamide, Y., et al. (1982), Global distribution of ionospheric and field-aligned currents during substorms as determined from six IMS meridian chains of magnetometers: Initial results, *J. Geophys. Res.*, *87*(A10), 8228–8240, doi:10.1029/JA087iA10p08228.
- Kim, H.-J., L. R. Lyons, J. M. Ruohoniemi, N. A. Frisell, and J. B. Baker (2012), Principal component analysis of polar cap convection, *Geophys. Res. Lett.*, *39*(11), L11105, doi:10.1029/2012GL052083.
- Koskinen, H. E. J., and E. I. Tanskanen (2002), Magnetospheric energy budget and the epsilon parameter, *J. Geophys. Res.*, *107*(A11), SMP-42-1–SMP-42-10, doi:10.1029/2002JA009283.
- Laundal, K. M., and J. W. Gjerloev (2014), What is the appropriate coordinate system for magnetometer data when analyzing ionospheric currents?, *J. Geophys. Res. Space Physics*, *119*(10), 8637–8647, doi:10.1002/2014JA020484.
- Laundal, K. M., et al. (2015), Birkeland current effects on high-latitude ground magnetic field perturbations, *Geophys. Res. Lett.*, *42*(18), 7248–7254, doi:10.1002/2015GL065776.
- Laundal, K. M., J. W. Gjerloev, N. Østgaard, J. P. Reistad, S. Haaland, K. Snekvik, P. Tenfjord, S. Ohtani, and S. E. Milan (2016), The impact of sunlight on high-latitude equivalent currents, *J. Geophys. Res. Space Physics*, *121*(3), 2715–2726, doi:10.1002/2015JA022236.
- Leopardi, P. (2007), Distributing points on the sphere: partitions, separation, quadrature and energy, PhD. Thesis, Univ. of New South Wales.
- Lockwood, M., S. W. H. Cowley, and M. P. Freeman (1990), The excitation of plasma convection in the high-latitude ionosphere, *J. Geophys. Res.*, *95*(A6), 7961–7972, doi:10.1029/JA095iA06p07961.

- Macmillan, S., and N. Olsen (2013), Observatory data and the Swarm mission, *Earth, Planets and Space*, *65*(11), 1355–1362, doi:10.5047/eps.2013.07.011.
- Maezawa, K. (1976), Magnetospheric convection induced by the positive and negative Z components of the interplanetary magnetic field: Quantitative analysis using polar cap magnetic records, *J. Geophys. Res.*, *81*(13), 2289–2303, doi:10.1029/JA081i013p02289.
- Matsuo, T., A. Richmond, and D. Nychka (2002), Modes of high-latitude electric field variability derived from DE-2 measurements: Empirical orthogonal function (EOF) analysis, *Geophys. Res. Lett.*, *29*(7), 1107, doi:10.1029/2001GL014077.
- Matsushita, S., J. D. Tarpley, and W. H. Campbell (1973), IMF sector structure effects on the quiet geomagnetic field, *Radio Sci.*, *8*(11), 963–972, doi:10.1029/RS008i011p00963.
- McGranaghan, R., D. J. Knipp, T. Matsuo, H. Godinez, R. J. Redmon, S. C. Solomon, and S. K. Morley (2015), Modes of high-latitude auroral conductance variability derived from DMSP energetic electron precipitation observations: Empirical orthogonal function analysis, *J. Geophys. Res. Space Physics*, *120*(12), 11,013–11,031, doi:10.1002/2015JA021828.
- McGranaghan, R., D. J. Knipp, and T. Matsuo (2016), High-latitude ionospheric conductivity variability in three dimensions, *Geophys. Res. Lett.*, *43*(15), 7867–7877, doi:10.1002/2016GL070253.
- McPherron, R. L., C. T. Russell, and M. P. Aubry (1973), Satellite studies of magnetospheric substorms on August 15, 1968: 9. Phenomenological model for substorms, *J. Geophys. Res.*, *78*(16), 3131–3149, doi:10.1029/JA078i016p03131.
- Milan, S. E., J. A. Carter, H. Korth, and B. J. Anderson (2015), Principal component analysis of birkeland currents determined by the active magnetosphere and planetary electrodynamics response experiment, *J. Geophys. Res. Space Physics*, *120*, 10,415–10,424, doi:10.1002/2015JA021680.
- Nishida, A. (1968a), Geomagnetic DP 2 fluctuations and associated magnetospheric phenomena, *J. Geophys. Res.*, *73*(5), 1795–1803, doi:10.1029/JA073i005p01795.
- Nishida, A. (1968b), Coherence of geomagnetic DP 2 fluctuations with interplanetary magnetic variations, *J. Geophys. Res.*, *73*(17), 5549–5559, doi:10.1029/JA073i017p05549.
- Perreault, P., and S. I. Akasofu (1978), A study of geomagnetic storms, *Geophys. J. Int.*, *54*(3), 547–573, doi:10.1111/j.1365-246X.1978.tb05494.x.
- Reiff, P. H., R. W. Spiro, and T. W. Hill (1981), Dependence of polar cap potential drop on interplanetary parameters, *J. Geophys. Res. Space Physics*, *86*(A9), 7639–7648, doi:10.1029/JA086iA09p07639.
- Richman, M. B. (1986), Rotation of principal components, *J. Climatol.*, *6*(3), 293–335, doi:10.1002/joc.3370060305.
- Richmond, A. D. (1995), Ionospheric electrodynamics using magnetic APEX coordinates, *J. Geomagn. Geoelectr.*, *47*(2), 191–212.
- Sabaka, T. J., N. Olsen, R. H. Tyler, and A. Kuvshinov (2015), CMS, a pre-Swarm comprehensive geomagnetic field model derived from over 12 yr of CHAMP, Ørsted, SAC-C and observatory data, *Geophys. J. Int.*, *200*(3), 1596–1626, doi:10.1093/gji/ggu493.
- Schunk, R. W., and A. Nagy (2009), *Ionospheres: Physics, Plasma Physics, and Chemistry*, Cambridge Univ. Press, Cambridge.
- Shore, R. M., K. A. Whaler, S. Macmillan, C. Beggan, J. Velmsk, and N. Olsen (2016), Decadal period external magnetic field variations determined via eigenanalysis, *J. Geophys. Res. Space Physics*, *121*(6), 5172–5184, doi:10.1002/2015JA022066.
- Stoneback, R. A., N. K. Malakar, D. J. Lary, and R. A. Heelis (2013), Specifying the equatorial ionosphere using CINDI on C/NOFS, COSMIC, and data interpolating empirical orthogonal functions, *J. Geophys. Res. Space Physics*, *118*(10), 6706–6722, doi:10.1002/jgra.50596.
- Sun, W., W.-Y. Xu, and S.-I. Akasofu (1998), Mathematical separation of directly driven and unloading components in the ionospheric equivalent currents during substorms, *J. Geophys. Res.*, *103*(A6), 11,695–11,700, doi:10.1029/97JA03458.
- Thébault, E., et al. (2015), International geomagnetic reference field: The 12th generation, *Earth, Planets and Space*, *67*(1), 1–19, doi:10.1186/s40623-015-0228-9.
- Thomson, A., C. Gaunt, P. Cilliers, J. Wild, B. Opperman, L.-A. McKinnell, P. Kotze, C. Ngwira, and S. Lotz (2010), Present day challenges in understanding the geomagnetic hazard to national power grids, *Adv. Space Res.*, *45*(9), 1182–1190, doi:10.1016/j.asr.2009.11.023.
- von Storch, H., and A. Navarra (1999), *Analysis of Climate Variability: Applications of Statistical Techniques: Proceedings of an Autumn School Organized by the Commission of the European Community on Elba from October 30 to November 6, 1993*, Springer, Berlin.
- von Storch, H., and F. Zwiers (2002), *Statistical Analysis in Climate Research*, Cambridge Univ. Press, Cambridge, U. K.
- Weimer, D. (2013), An empirical model of ground-level geomagnetic perturbations, *Space Weather*, *11*(3), 107–120.
- Weimer, D. R. (1994), Substorm time constants, *J. Geophys. Res.*, *99*(A6), 11,005–11,015, doi:10.1029/93JA02721.
- Weimer, D. R. (2005a), Improved ionospheric electrodynamic models and application to calculating Joule heating rates, *J. Geophys. Res.*, *110*(A5), A05306, doi:10.1029/2004JA010884.
- Weimer, D. R. (2005b), Predicting surface geomagnetic variations using ionospheric electrodynamic models, *J. Geophys. Res.*, *110*, A12307, doi:10.1029/2005JA011270.
- Weimer, D. R., C. R. Clauer, M. J. Engebretson, T. L. Hansen, H. Gleisner, I. Mann, and K. Yumoto (2010), Statistical maps of geomagnetic perturbations as a function of the interplanetary magnetic field, *J. Geophys. Res.*, *115*, A10320, doi:10.1029/2010JA015540.
- Xu, W. Y., and Y. Kamide (2004), Decomposition of daily geomagnetic variations by using method of natural orthogonal component, *J. Geophys. Res. Space Physics*, *109*, A05218, doi:10.1029/2003JA010216.